Fluid Dynamics &
Materials Processing

Tech Science Press

http://doi.org/10.32604/fdmp.2026.075928

ARTICLE

Oblique Magneto-Thermal Flow with Non-Fourier Heat Transfer over a Radiative Rotating Disk

Abdou Alzubaidi[1], Khalid Mahmud[2], Rashid Mehmood[2,*], Siddra Rana[3] and Mohammed Alkinidri[4]

[1]Department of Mathematics, College of Sciences, King Khalid University, Abha, Saudi Arabia
[2]Department of Mathematics, Faculty of Natural Sciences, HITEC University, Taxila Cantt, Taxila, Pakistan
[3]Department of Mathematics, Faculty of Basic Sciences, University of Wah, Wah Cantt, Pakistan
[4]Department of Mathematics, College of Science & Arts, King Abdulaziz University, Rabigh, Saudi Arabia
*Corresponding Author: Rashid Mehmood. Email: rashid.mehmood@hitecuni.edu.pk

Received: 11 November 2025; Accepted: 06 March 2026; Published: 07 May 2026

ABSTRACT: Flows over rotating disks are central to numerous engineering applications, including turbines, rotating sensors, and advanced cooling devices, where the incoming fluid often strikes the disk at an angle. This study examines magnetohydrodynamic (MHD) oblique slip flow toward a rotating disk, accounting for critical effects such as velocity slip, thermal slip and thermal radiation. In particular, the Cattaneo–Christov heat flux model is used to capture thermal relaxation phenomena, frequently overlooked in prior analyses, while employing a uniform transverse magnetic field to regulate both momentum and heat transfer. Using similarity transformations, the governing nonlinear equations are reduced to ordinary differential equations and solved through a shooting method combined with a robust finite-difference scheme. Three-dimensional streamline visualizations are exploited to elucidate the influence of slip and oblique incidence on the near-disk flow structure. The results reveal three principal effects: the rotational flow intensifies near the disk surface, the stagnation point shifts with velocity slip, and the main-flow velocity increases while cross-flow velocity diminishes as slip rises. Thermal analysis indicates that the boundary-layer temperature decreases under thermal slip and radiation, whereas local heat transfer is significantly enhanced. Furthermore, the skin-friction coefficient grows with disk rotation speed but declines with higher velocity slip, highlighting the coupled influence of rotational and slip effects on overall momentum and heat transfer.

KEYWORDS: Slip oblique flow; rotating disk; Cattaneo-Christov: magneto hydrodynamics; heat transfer; 3D stream patterns

1 Introduction

Fluid flows induced by rotating disks remain a focal point of contemporary research due to their extensive applications across various scientific and engineering disciplines. This topic is of significant interest to researchers and manufacturers involved in the design of gas turbine rotors, thermal power systems, medical equipment, rotary plating, electronic storage devices, and swirling purification systems. In nature, rotating flows are observed in phenomena ranging from tornadoes, hurricanes, and oceanic circulation to spiral galaxies and everyday occurrences like the vortex in a draining bathtub. However, the description of rotational flow extends beyond simple observation. Von Kármán [1] pioneered the investigation of flow over an infinite rotating disk. By exploiting classical transformations, he successfully reduced the governing Navier-Stokes equations into a system of ordinary differential equations. His groundbreaking study served as the foundation for numerous subsequent investigations into rotating flow

problems from various engineering perspectives. Building on this, Lok et al. [2] examined fluid striking a stretching sheet at a specific angle. They discovered that the stagnation point shifts toward the incoming fluid flow due to free stream obliqueness, a behavior dependent on the angle of inclination. Nadeem et al. [3] explored oblique flow toward a stretched surface with heat transfer, observing that heat transfer is directly related to the elasticity parameter and inversely proportional to thermophoresis and Brownian motion. Furthermore, while mass transfer increases with the viscoelastic parameter and Brownian motion, it decreases as thermophoresis increases. Rashid et al. [4] examined the transfer of oblique flow over a stretching plate, highlighting that local skin friction coefficients decrease as the stretching ratio enhances. Conversely, mass flux and local heat at the stretching surface decline when the stretching ratio increases. Sarkar [5] studied non-orthogonal stagnation point flow over a rotating disk, noting that the rotational parameter and the azimuthal velocity component are inversely proportional.

A frequently occurring condition in rotating disk structures is forced flow along the same axis as the disk. This scenario has critical real world applications, including chemical reactions, spinning blades, and silicon wafer cooling. Most prior studies assumed that stagnation point flow was axisymmetric and parallel to the axis of the revolving disk. However, this assumption does not hold in all realistic scenarios, as fluids may occasionally collide obliquely at an arbitrary angle of inclination. Recent research has expanded to include complex fluid models. Jawad et al. [6] investigated the rotational stagnation-point flow of a Maxwell nanofluid across a porous, radially expanding and contracting rotating disk. They found that the rate of heat transmission increases as the thermophoresis parameter decreases. In a related study, Jawad et al. [7] considered Oldroyd-B fluid (a subclass of non-Newtonian fluid) and analyzed the effects of convective boundary conditions and non-linear thermal radiation. Mahanthesh et al. [8] focused on visualizing the nonlinear radiated flow of a hydromagnetic nanofluid, testing various nanoparticle shapes such as lamina, cylinder, and pyramid.

For the first time, Andersson et al. [9] discussed Newtonian slip flow caused by a lubricated rotating disk and observed that torque needed to keep the disk rotating steadily and to maintain pumping effectiveness decreases monotonically with an increase in slip. Imtiaz et al. [10] investigated the effects of magnetohydrodynamics on slip flow toward a rotating disk of varied thickness. It has been noted that axial and radial velocities effect the thickness coefficient of the disk in opposing ways, and further surface drag force and Hartman number are also directly related. At the axial and radial velocities, thickness coefficient of disk exhibits opposite behaviour. Mustafa [11] examined partial slip effects on MHD nano fluid flow towards a rotating disk. It has been highlighted that the velocity slip coefficient and the intensity of the magnetic field are decreasing functions of azimuthal, axial, and radial velocities. When the conventional no-slip assumption fails, particularly at very small scales or in rarefied environments, sliding occurs at solid borders. In these situations, the fluid might move slightly in relation to the solid due to weak interactions between the fluid and the surface, producing a finite tangential velocity known as slip [12]. In confined flows or ones with large Knudsen numbers, this modification modifies shear stress and heat transfer behavior by affecting the velocity gradients close to the wall. Studies of slip in rotating-disk configurations, such as flow between co-rotating disks with heat transfer, reveal that slip affects both the flow dynamics and surface heat fluxes within these rotating systems. The effect of the presence of wall slip significantly reduces the opposing torque on the disk. Reiner-Rivlin nanofluid slip flow towards a rotating disk was investigated numerically by Naqvi et al. [13]. It is observed that a decrease in radially outward flow is brought on by a rise in the Reiner-Rivlin parameter. When there is a decline in skin friction and driving torque, greater viscoelastic effects are seen. In contrast to entrainment velocity, skin friction and resisting torque increase with a rise in the values of the parameters of wall roughness. The wall roughness parameter has an inverse relation

with the radial velocity profile. Majeed et al. [14] studied the heating in a stenotic artery by considering the Darcy-Forchheimer model. It was determined that for nanoparticle fraction of volume, velocity, and temperature, they display comparable behaviour, and higher velocity slip parameters cause speed reduction. It is observed that there is a temperature decline for thermal slip. When the Forchheimer number and the velocity slip variable are present, the coefficient of skin friction is greater. Due to the presence of thermal slip, the local Nusselt number is increased. Khan et al. [15] investigated the nonlinear thermal radiation, stimulation energy, and slip flow of a permeable rotational disk filled with a micropolarthe nanofluid that contained active microbes. It is observed that the slip parameter successfully controls the growing velocity variation. Shoaib et al. [16] examined the heat-transfer properties in an MHD hybrid nanofluid flow brought on by the exchange of heat from the disk that rotates, as well as the flow of a 3D hybrid nanofluid over a rotating disk with a uniform magnetic field of flow. When Zemedu et al. [17] examined the stable, smooth, dual-dimensional boundary layer flow of a nonlinear convection-driven micropolar nanofluid caused by a spinning disk, they discovered that increasing the thermal and solutal nonlinear convection-based coefficients could increase the radial velocity close to the disk top while decreasing the velocities away from the disk. Rafiq et al. [18] wanted to explore the convective heat transport and magnetohydrodynamics (MHD) hybrid nanofluid flow via a stretchy spinning surface using the Yamada-Ota and Xue models with the consequences of heat generation and thermal radiation. They determined that within a specific range of unsteadiness parameters, two solution branches are obtained. Increasing the impacts of thermal radiation and heat generation increases the fluid temperature and rate of heat transfer. When the stability analysis is applied, it is found that only the first solution is still stable.

Thermal radiation is a very important effect in situations where conduction and convection alone cannot explain energy transport, particularly at high temperatures. It dominates processes in gas turbines, combustion chambers, nuclear reactors, aerospace vehicle design, and solar energy collection. Adding radiation to fluid flow analysis gives more accurate heat transfer predictions, especially when handling high-temperature rotating surfaces. A widespread phenomenon in nature is heat transfer, which occurs when there are temperature differences between two objects. Turkyilmazoglu [19] studied the transfer of heat of nanofluid flow with thermal radiation and used the finite element technique for simulation. It is noted that radial and angular velocities near the disk diminished as the nanoparticle's volume fraction parameter increased for the nanofluid. Additionally, it is observed that an increase in the volume percentage of nanoparticles leads to increased heat output, and hence, the thermal layer thickness is also increased. Abbas et al. [20] examined their work in a comparative study of heat transfer processes in the thermal boundary layer over an infinite rotating disk. The nanoparticles are covered with a water-based fluid that is exposed to thermal radiation. The finite difference-based approach bvp4c was used to numerically solve the derived non-linear ODEs. The results showed that suction dampens the variation and lessens the velocity overshoot. The radiation effect's existence led to temperature drops in the fluid and an increase in the Nusselt number. With a rise in magnetic field strength, it was shown that the tangential component of the surface's skin friction increases while the skin's radial friction, heat, and coefficients of mass transfer all decrease. It is noted that with the rise of the Prandtl number, the mass transfer coefficient drops while the heat transfer coefficient increases. Khedher et al. [21] discussed thermal and electro-osmotic energy transport in complex peristaltic flows. Thermal diffusivity has an inverse relationship with the Prandtl parameter. Higher Prandtl parameter estimates indicate less thermal diffusivity, which results in a decrease in temperature distribution [22]. Song et al. [23] considered an off-centered rotating disk for examining the thermal radiation by using bioconvection flow of micropolar nanofluid. It is highlighted that for the parameter of thermophoresis, the concentration of species increases, and the concentration

of nanoparticles declines with increasing Prandtl number. It is also noted that the Prandtl number has a decreasing relationship with the microorganism field.

The Fourier law, classical in formulation, postulates instantaneous heat propagation, which is not physically realistic for ultrafast heating, microscale heat transfer, or high-frequency thermal processes. The Cattaneo–Christov model, among others, has a relaxation time parameter to capture finite thermal wave speed and delay phenomena. This results in a better description of transient heat conduction, particularly in materials with quick thermal responses, laser heating, and nanoscale systems. Fourier [24] defined the heat conduction law in 1822. Fourier's law misconceptions were removed by Cattaneo [25] by introducing a new heat flux model, and then Christov [26] improved it. Tangential velocity is seen to increase when stretching and rotational factors increase, and both the Prandtl number and parameter of thermal relaxation cause a decrease in temperature. Additionally, it is noted that for greater rotational parameters, force of surface drag at both disks is reduced. Doh et al. [27] considered the heat flux model by Cattaneo-Christov to analyse the 3D magnetohydrodynamic flow of a micropolar fluid between two stretched rotating disks, and it was noted that as the unsteadiness parameter is increased, inward axial velocity, tangential, radial, and inward axial micro-rotational velocity profiles decline, and velocity profiles of radial micro-rotational rise. It is highlighted that with increasing thermal relaxation parameters, the temperature profile is significantly reduced. In the article, the influence of Brownian motion and thermophoresis on the flow and heat transfer characteristics of Maxwell nanofluids flowing across a stretching plate is explored by Saeed et al.'s [28]. They suggested potential ways to improve performance in heat exchange applications by highlighting the role that nanoparticle characteristics play in determining the efficacy of heat transfer operations. Gholinia et al. [29] discussed fluid flow over a vertical circular cylinder having a sinusoidal radius. It is noted that velocity along the radial direction enhances with higher values of the ratio between relaxation and retardation, and also it is reversed along the tangential direction. It is also observed that with respect to the Deborah number, radial and tangential velocities are directly related, and increased retardation time results in improved elasticity. The study of Jeffrey fluid axisymmetric flow towards a rotating disk with varying surface thickness is done by Imtiaz et al. [30] with the Cattaneo–Christov heat flux model. Tulu et al. [31] studied the carbon nanoliquid flow for a stretchable rotating disk by considering the Cattaneo–Christov heat flux model. Hafeez et al. [32] studied the von Karman whirling flow of magnetized viscoelastic Oldroyd-B fluid driven by a rotating disk by using the double-diffusion model by Cattaneo-Christov. Higher stretching parameter values are seen to increase velocity in the radial direction while decreasing velocity in the azimuthal direction. Additionally, it has been observed that as the velocity ratio parameter is increased, the radial and azimuthal speeds decrease. Using the Cattaneo-Christov heat flux theory. Additionally, as the thermal relaxation period increased, the fluid temperature declined. It is also observed that, as compared to a homogeneous reaction rate, the wall concentration gradient is reduced. Some recent literature can be reviewed regarding the current study [33–36].

In this work, magnetohydrodynamic oblique slip flow across a radiative rotating disk under non-Fourier thermal diffusion is investigated in a novel way. The current analysis includes oblique slip at any angle in conjunction with the Cattaneo–Christov non-Fourier model, in contrast to previous publications that mainly examined axial or radial slip with Fourier's equation of heat transportation. Previously unexplored in the literature, the combination of radiative heat transfer and non-Fourier thermal relaxation with the generation of entropy analysis offers fresh perspectives on energy-efficient thermal transport in spinning disk systems. This study's originality is described by the obliqueness Parameter brought about by the external shear term, a measurement of the external flow's arbitrary-angle impingement on a revolving disk. This is the shear-driven oblique stagnation flow, which has never before been combined with non-Fourier

heat conduction, slip, and thermal radiation. Velocity slip shows finite slip on the spinning surface, which is applicable at the micro/nanoscale or on lubricated surfaces. Additionally, heat flux and temperature gradients are changed by the finite thermal jump at the wall, which is captured by the thermal slip parameter. Cattaneo-Christov. In the context of a spinning disk system under oblique stagnation flow, the term "relaxation" refers to the effects of thermal relaxation. The parameter of radiation is a novel mix of nonlinear Rosseland radiation and Cattaneo-Christov theory.

The paper is organised in the manner described below. An introduction and a review of the literature are included in Section 1. The proposed problem's mathematical modelling is explained in detail in Section 2. Section 3 presents a solution presented in the form of graphs and a physical interpretation of the results. Finally, Section 4 offers final findings.

2 Mathematical Formulation

This study examines the constant flow of a 3-D viscous fluid that impinges longitudinally on an infinitely rotating disk in the xy–plane. The notation Ω is used to indicate angular velocity, which is assumed to be constant, and fluid volume, which is assumed to be $z > 0$. It is assumed the (x, y, z) are defined Cartesian coordinate system, where the x-axis and the y-axis are defined along the disk's surface, and the z-axis is taken perpendicular to the disk. Furthermore, they (u, v, w) are defined as velocity components in (x, y, z) directions, as seen in Fig. 1.

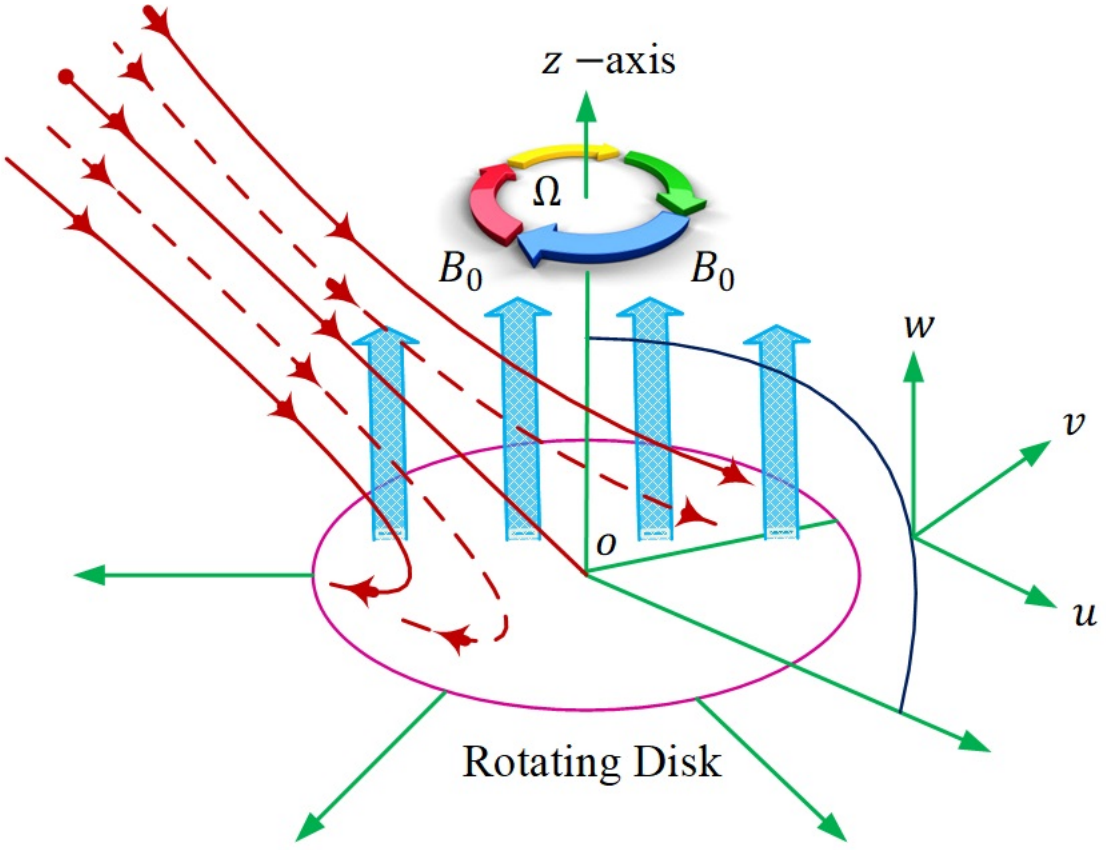

Figure 1: Flow configuration schematic diagram: An external uniform magnetic field B_0 is applied to a revolving disk with angular velocity Ω. The radial, tangential, and axial velocity components are represented by the coordinate axes (u, v, w). The entering oblique free-stream flow (u_e, v_e, w_e) interacts with the boundary layer as it approaches the disk surface at an angle.

Now, we have taken the fluid flow [2,5,37]:

$$(u_e, v_e, w_e) = (ax + bz^{\frac{1}{2}}, ay, -2az), \quad T = T_\infty \quad \text{at} \quad z \to \infty \tag{1}$$

The irrotational stagnation strain rate is represented by the constant a, whereas the additional shear strain rate applied in the x-direction is represented by constant b. An asymmetric stagnation area is produced by this shear component, which models the obliqueness of the entering flow. As in the wall stretching in magnetohydrodynamics rotating flows in inertial and rotating frames, the exterior flow turns into the traditional orthogonal stagnation flow of the rotating-disk experiments when $b = 0$. The shear-deformation of the external flow that results in the inclined stagnation-point behavior is thus described by the phrase $\frac{1}{2}bz^{\frac{1}{2}}$ [38]. The system of equations that results under those conditions is as follows [19,24–26,39]:

$$u_x + v_y + w_z + = 0 \tag{2}$$

$$uu_x + vu_y + wu_z = \nu\nabla^2 u - \frac{1}{\rho}p_x - \frac{\sigma B_0^2 u}{\rho} \tag{3}$$

$$uv_x + vv_y + ww_z = \nu\nabla^2 v - \frac{1}{\rho}p_y - \frac{\sigma B_0^2 v}{\rho} \tag{4}$$

$$uw_x + vw_y + ww_z = \nu\nabla^2 w - \frac{1}{\rho}p_z \tag{5}$$

$$uT_x + vT_y + wT_z = \left(\frac{K}{\rho C_p} + \frac{16\sigma^* T_\infty^3}{3k^*\rho C_p}\right)\nabla^2 T$$
$$-\lambda\left[u^2 T_{xx} + w^2 T_{zz} + 2uwT_{xz}\right] = -\lambda[T_x(uu_x + wu_z) + T_z(uw_x + ww_z)] \tag{6}$$

where the kinematic viscosity, density, pressure, and temperature are represented by ν, ρ, P, and T, respectively. The conditions on the disc are defined by the Eq. (7). For heat flux, the Cattaneo–Christov constitutive law is: $q + \lambda\nabla q = -k\nabla T$, where λ is the thermal relaxation term and ∇q is the upper convected derivative. Using this Catteneo-Christovo term in the energy equation, since for rotating-disk flows, boundary-layer approximations are frequently utilized. Since there is no variation in the y direction $\frac{\partial}{\partial y} \to 0$. There are dominant gradients in the x- and z-directions, so ignore higher-order terms like u_y and v_z. Following the application of these simplifications, getting the advection term, i.e., the left-hand side, the first term of Eq. (6) $uT_x + vT_y + wT_z$ and the classical Fourier diffusion term, the second term on the right-hand side in Eq. (6) $\left(\frac{K}{\rho C_p} + \frac{16\sigma^* T_\infty^3}{3k^*\rho C_p}\right)\nabla^2 T$, the second term comes from Rosseland radiative heat flux approximation. Christov correction (relaxation effects) is given by the upper-convected derivative, which gives the extra terms $-\lambda\left[u^2 T_{xx} + w^2 T_{zz} + 2uwT_{xz}\right]$ and from the velocity gradient contributions is $-\lambda[T_x(uu_x + wu_z) + T_z(uw_x + ww_z)]$. By combining these two terms, we get Eq. (6).

$$u = -\Omega y + \lambda_1\frac{\partial u}{\partial z}, \quad v = -\Omega x + \lambda_2\frac{\partial u}{\partial z}, \quad w = 0, \quad T = T_w \quad \text{at} \quad z = 0 \tag{7}$$

where physically the boundary conditions explain the disk's rigid-body rotation, denoted by the equations $-\Omega y$ and $-\Omega x$, causing the fluid to be dragged in an azimuthal direction by viscous action. The fluid does not completely cling to the disk surface under these Navier slip boundary conditions. Micro/nanoscale flows, lubricated disks, and surfaces with weak fluid–solid contact forces can all experience velocity slip. Condition of no penetration Since the disk is impermeable, there is no normal velocity at the surface. The condition of temperature ensures that, in line with thermal-control applications, the disk's surface

temperature remains constant. Far-field conditions guaranteed that the external flow is unaffected far from the surface and that the rotating disk solely affects the boundary layer. When combined, these boundary conditions depict a physically plausible interaction between an obliquely impinging slip-flow environment and a revolving disk. Eqs. (2)–(6) simplified to the following equations considering large z

$$-\frac{1}{\rho}\frac{\partial P}{\partial x} = u_e\frac{\partial u_e}{\partial x} + w_e\frac{\partial u_e}{\partial z} + \frac{\sigma B_0^2 u_e}{\rho} \tag{8}$$

$$-\frac{1}{\rho}\frac{\partial P}{\partial y} = v_e\frac{\partial v_e}{\partial y} + \frac{\sigma B_0^2 v_e}{\rho} \tag{9}$$

$$-\frac{1}{\rho}\frac{\partial P}{\partial z} = w_e\frac{\partial w_e}{\partial z} \tag{10}$$

$$w\frac{\partial T}{\partial z} = \left(\frac{K}{\rho C_p} + \frac{16\sigma^* T_\infty^3}{3k^*\rho C_p}\right)\frac{\partial^2 T}{\partial z^2} - \lambda\left[w^2\frac{\partial^2 T}{\partial z^2} + w\frac{\partial w}{\partial z}\frac{\partial T}{\partial z}\right] \tag{11}$$

which convert the governing heat transport and momentum conservation laws into:

$$u_x + v_y + w_z = 0 \tag{12}$$

$$uu_x + vu_y + wu_z = u_e u_{ex} + w_e u_{ez} + \nu\nabla^2 u + \frac{\sigma B_0^2 u_e}{\rho} - \frac{\sigma B_0^2 u}{\rho} \tag{13}$$

$$uv_x + vv_y + wv_z = v_e v_{ex} + \nu\nabla^2 v + \frac{\sigma B_0^2 v_e}{\rho} - \frac{\sigma B_0^2 v}{\rho} \tag{14}$$

$$uw_x + vw_y + ww_z = w_e w_{ez} + \nu\nabla^2 w \tag{15}$$

$$wT_z = \left(\frac{K}{\rho C_p} + \frac{16\sigma^* T_\infty^3}{3k^*\rho C_p}\right)\frac{\partial^2 T}{\partial z^2} - \lambda\left[w^2 T_{zz} + ww_z T_z\right] \tag{16}$$

The case of a disk with no rotation is the axisymmetric oblique stagnation point flow that was derived from the previous set of equations for $\Omega = 0$. This approach works quite well for resolving PDEs of this type that arise in boundary layer flow issues. The following list of similarity transformations has been applied.

$$\left.\begin{aligned} U = (u, v, w) &= (axf' - \Omega yg + (a\nu)^{1/2}h, ayf' - \Omega x, -2(a\nu)^{1/2}f) \\ \theta &= \frac{T - T_\infty}{T_w - T_\infty}; \quad \zeta = (\frac{a}{\nu})^{1/2}z. \end{aligned}\right\} \tag{17}$$

where $f = f(\zeta), g = g(\zeta), h = h(\zeta)$ and $\theta = \theta(\zeta)$. The similarity variables are selected according to the classical Karman scaling: the thickness of the boundary layer scales as $\delta \sim (\frac{a}{\nu})^{1/2}$, so $\zeta = (\frac{a}{\nu})^{1/2}z$. The velocity decomposition separates the linear x, y dependence of the outer inviscid flow from the viscous ζ dependent correction and continuity. Replacing these forms in the non-dimensionalized version of the Navier-Stokes and Cattaneo-Christov equations of energy non-dimensionalizing with the scales a and $(a\nu)^{1/2}$ eases the PDEs to the ODE system. The Navier slip and thermal jump over the disk lead to the boundary conditions at $\zeta = 0$ and equal to the induced external stagnation field as $\zeta \to \infty$. Such reductions of similarity are regular with the classical von Karman and oblique-stagnation similarity processes and retrieve the usual limits in case of $\alpha, \gamma, \delta_1, \delta_2 \to 0$

The obtained systems of PDEs from Eq. (13) through Eq. (16) become:

$$f''' + 2ff'' - f'^2 + 1 + \alpha^2 g^2 + M^2 - M^2 f' = 0 \tag{18}$$

$$g'' + 2fg' - 2gf' - M^2 g = 0 \tag{19}$$

$$h'' + 2fh' - hf' - M^2 h + M^2 \gamma \zeta^{\frac{1}{2}} = 0 \tag{20}$$

$$\frac{1}{\Pr}(1 + R_d)\theta'' + 2f\theta' - 4\beta[ff'\theta' + f^2\theta''] = 0 \tag{21}$$

This reduces boundary conditions to

$$f = 0, \quad f' = \delta_1 f''(\zeta), \quad g = 1 + \delta_1 g'(\zeta), \quad h = \delta_1 h'(\zeta), \quad \theta = 1 + \delta_2 \theta'(\zeta) \quad \text{at} \quad \zeta = 0 \tag{22}$$

$$f' = 1, \quad g = 0, \quad h = \gamma \zeta^{\frac{1}{2}}, \quad \theta = 0 \quad \text{at} \quad \zeta \to \infty \tag{23}$$

Here the rotational ratio parameter is represented by α and $\alpha = \frac{\Omega}{a}$, obliqueness parameter by $\gamma = \frac{b}{\sqrt{a}} \frac{1}{(a\nu)^{\frac{1}{4}}}$, M is Magnetic field parameter with $M^2 = \frac{\sigma B_0^2}{\rho a}$ and β is thermal relaxation parameter by and $\beta = \lambda\, a$. Taking into account $\alpha = 0$, the flow on a wall is represented by the Eqs. (18)–(21) and their boundary conditions Eqs. (22) and (23), which are applicable in non-orthogonal stagnation point flow. In Eq. (18) through Eq. (21) and its boundary conditions (22) and (23), which define this flow towards a spinning disc, substitute $b = 0$ when the stagnation point flow is axisymmetric orthogonal. The following are the components of wall shear stress:

$$\tau_\chi = \rho\nu u_z|_{z=0} = a\rho\nu[\chi f''(\zeta) - \alpha\zeta g'(\zeta) + h'(\zeta)]|_{\zeta=0} \tag{24}$$

$$\tau_\zeta = \rho\nu v_z|_{z=0} = a\rho\nu[\zeta f''(\zeta) + \alpha\chi g'(\zeta)]|_{\zeta=0} \tag{25}$$

At the shear stress point, the shear is zero. With $\tau_\chi = 0$ and $\tau_\zeta = 0$, for example, we achieved the shear center when shear is zero.

$$\rho\nu u_z|_{z=0} = a\rho\nu[\chi f''(\zeta) - \alpha\zeta g'(\zeta) + h'(\zeta)]|_{\zeta=0} = 0 \tag{26}$$

$$\rho\nu v_z|_{z=0} = a\rho\nu[\zeta f''(\zeta) + \alpha\chi g'(\zeta)]|_{\zeta=0} = 0 \tag{27}$$

From Eqs. (26) and (27),

$$\chi_s = -\frac{f''(\zeta)h'(\zeta)}{(f''(\zeta))^2 + \alpha^2(g'(\zeta))^2}\bigg|_{\zeta=0}, \qquad \zeta_s = -\frac{\alpha h'(\zeta)g'(\zeta)}{(f''(\zeta))^2 + \alpha^2(g'(\zeta))^2}\bigg|_{\zeta=0} \tag{28}$$

and the temperature gradient at the disc surface is

$$-T_y|_{y=0} = -\theta'(\zeta)\big|_{\zeta=0} \tag{29}$$

In order to make the numerical scheme which is defined in Fig. A1 reliable, the model was tested for some of the well-known limiting cases, for $\gamma = 0 = \delta_1 = \delta_2 = \beta = Rd$. The current equation simplifies to the classical von Karman rotating disk equation. The computed values of $f''(0), g'(0), \theta'(0)$ concide with

the benchmark rotating-disk solutions of [40], Mehmood and Usman [41] and Shevchuk [42] and have errors less than 1%.

Parameter	[40]	[41]	[42]	Present Results
$f''(0)$	0.510	0.5102	0.5102	0.5102
$-g'(0)$	0.615	0.6159	0.6159	0.6159
$-\theta'(0)$	0.395	0.3969	0.3969	0.3969

3 Numerical Results and Discussion

Several physical parameters, including the magnetic field parameter M, the velocity slip parameter δ_1, the thermal slip parameter δ_2, the obliqueness parameter γ, the thermal radiation parameter Rd, and the Prandtl number Pr, are compared to the heat transfer and flow features of the modeled mathematical problem. The findings are quite optimistic.

We are therefore very confident of our subsequent graphical results. Fig. 2 illustrates a streamlined pattern $xy\zeta$-plane in the absence of rotation, i.e., for the case of a stationary disk. Orthogonal ($\gamma = 0$) and oblique ($\gamma \neq 0$), for both cases, are represented by different values of the velocity slip parameter δ_1. It can be seen from the streamline profiles that the field of flow shows a strong inclination relative to the stagnation point as a function of the obliqueness parameter value γ. Since it γ is an obliqueness parameter, which is the angle of attack of flow towards the disk, and it has different impacts for positive, negative, and zero values. For positive values of γ, the streamlines deviate in the direction of negative x-axis, which signifies the directional skewness in the flow structure close to the stagnation point. The flow becomes oblique, towards the negative x direction. Since the streamlines are perpendicular to the inflow velocity, the streamlines are inclined in the negative x-direction. In contrast, negative values of γ reverse this trend, changing the streamline direction towards the positive x-axis. Additionally, the size γ is instrumental in controlling the level of flow deflection. The horizontal element of the incoming flow is now directed to a positive x-direction; hence, the streamlines bend towards the positive x. This opposes the tendency of the flow and creates a skewness of opposite nature in the stagnation-point structure. When γ is increased, the streamlines become increasingly sloped, indicating a rise in obliqueness of impinging flow in the same direction as the rotating disk. In physical terms, this means that higher values of γ strengthen the non-symmetric stagnation-point flow, changing pressure and velocity distributions along the surface. These changes are significant, since they have a direct bearing upon transport phenomena such as momentum transfer and heat exchange in the boundary layer. The streamline pattern for a rotating disk is depicted in the $xy\zeta$-plane in the Fig. 3 by taking the obliqueness parameter $\gamma = -1, 0, 1$ for a constant velocity slip $\delta_1 = 2$ parameter. It is no longer possible to have the fluid stick to the disk perfectly. The lower shear of the wall is due to decreased surface resistance. This enables the flow in direction to enter more freely to the oblique direction imposed. Therefore, slip increment augments inclination with streamlines and intensifies the skewness of the observed streamlines.

Thermally, the greater the slip, the smaller the frictional heating, and the greater the intensity of local convection; hence, the increase in surface heat flux with high slip values. The angular velocity Ω of the rotating disk is assumed to remain constant. This disk revolution in turn causes the fluid to rotate, which generates the centrifugal force, which is a force acting radially outward. This $3D$ flow is a pump based on continuous phenomena; the term “free disk pumping effect” [39] is the most commonly used to describe it. It is consistent with the fact that efflux is a greater outward force flow. Since the stagnation point has the highest pressure, rotational motion is produced around it.

To understand the properties of the velocity profiles, $f'(\zeta)$ and $g(\zeta)$, curves are shown for different values of the velocity slip parameter δ_1. Fig. 4 is plotted for different values of the velocity slip parameter δ_1 to examine its effect on primary velocity $f'(\zeta)$, and it is highlighted that the velocity component enhances with the velocity slip parameter. Fig. 5 shows a graph for the induced velocity for different values of the velocity slip parameter, $g(\zeta)$, and it is observed that the induced velocity decreases with the velocity slip parameter δ_1. The rotating disk pushes the fluid around in the rotational direction by the influence of viscosity. In this spinning fluid, there is an outward centrifugal force that generates the rise in radial velocity off-center. Classical von Karman rotating-disk boundary layer Suction-like upward movement. The stream is symmetrical around the center. The stagnation point is still at the center, and the rotation is prevailing in radial spreading. The oblique driving force causes the stagnation area to be pushed on the negative $x$side. This momentum is then carried off asymmetrically during rotation, which continues to distort the structure of the boundary layer. The sign of tilt is opposite to that of g. Since the rotation will create a circulation that moves around the stagnation zone, the oblique inflow will interact with the circulation, creating visible swirling patterns. The swirling is observed towards the stagnation point due to the reason that the rotational disk is causing azimuthal (tangential) velocity. This causes a secondary vortex-like pattern of the stagnation point with the highest pressure. The flow of incoming oblique alters this vortex and reinforces or weakens it by the sign of g.

It is this outward acceleration that causes the so-called free-disc pumping effect: rotating pumps the fluid at the center of the fluid toward the outer parts. The fluid's temperature $\theta(\zeta)$ and the degree of thickness of the thermal boundary layer reduce with the velocity slip constant δ_1, as shown in Fig. 6. Fig. 7 shows the effect of the rotation ratio parameter α and Prandtl number on the coefficients of skin friction, $(f''(0)$, and it is observed that the coefficient of skin friction enhances with the rotation ratio parameter α. Fig. 8 is plotted to examine the effect of the rotation ratio parameter α on local heat flux $(\theta'(0))$, and local heat flux decreases with an increase in the rotation ratio parameter α. Local heat flux $(\theta'(0))$ against the thermal slip parameter δ_2 for different values of the Prandtl number Pr is depicted through the graph shown in Fig. 9, and it reveals that local heat flux decreases with a rise in Prandtl number values. Fig. 10 exhibits that $\theta'(0)$ against the coefficient of thermal radiation R for different values of the Prandtl number, Pr, and it enhances at the surface of the rotating disk.

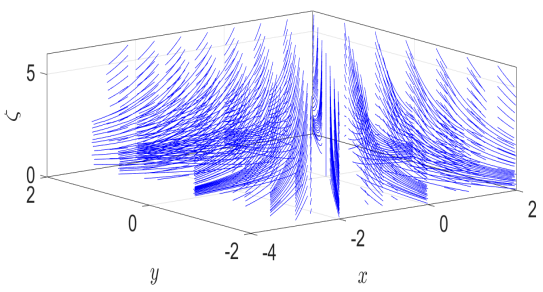

(a) $\alpha = 0, \delta_1 = 0, M = 2, \gamma = 0$

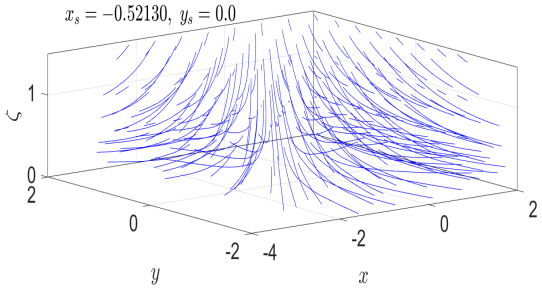

(b) $\alpha = 0, \delta_1 = 0, M = 2, \gamma = 1$

Figure 2: *Cont.*

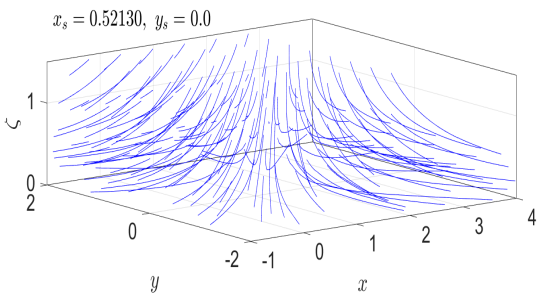

(c) $\alpha = 0, \delta_1 = 0, M = 2, \gamma = -1$

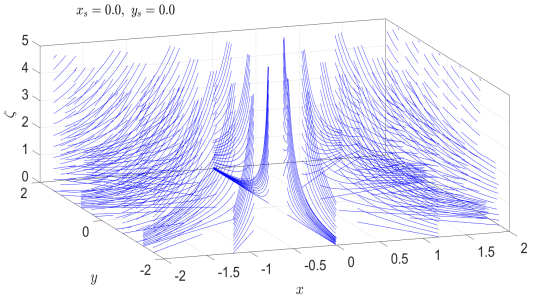

(d) $\alpha = 0, \delta_1 = 2, M = 2, \gamma = 0$

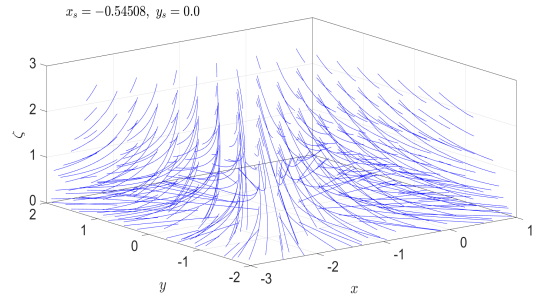

(e) $\alpha = 0, \delta_1 = 2, M = 2, \gamma = 1$

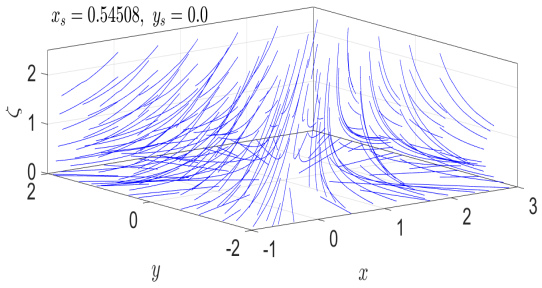

(f) $\alpha = 0, \delta_1 = 2, M = 2, \gamma = -1$

Figure 2: Streamlines for $\alpha = 0$ for obliqueness parameter γ and velocity slip parameter δ_1.

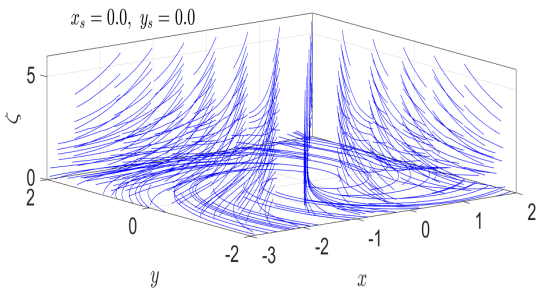

(a) $\alpha = 1, \delta_1 = 2, M = 2, \gamma = 0$

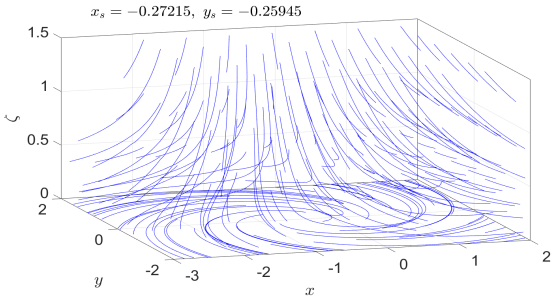

(b) $\alpha = 1, \delta_1 = 2, M = 2, \gamma = 1$

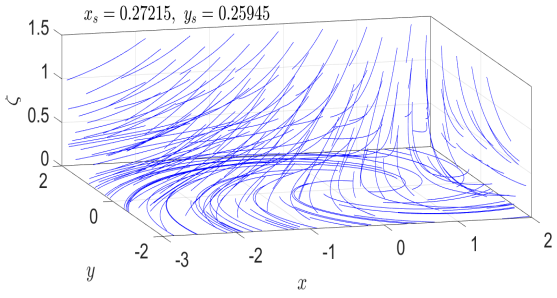

(c) $\alpha = 1, \delta_1 = 2, M = 2, \gamma = -1$

Figure 3: Streamlines for $\alpha = 1$ for obliqueness parameter γ.

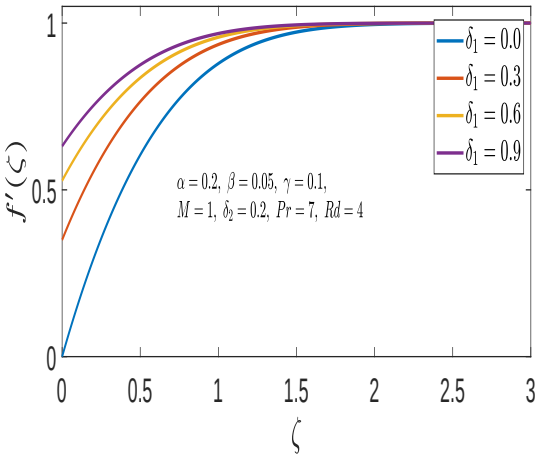

Figure 4: Velocity profile $f'(\zeta)$ for various values of velocity slip parameter δ_1.

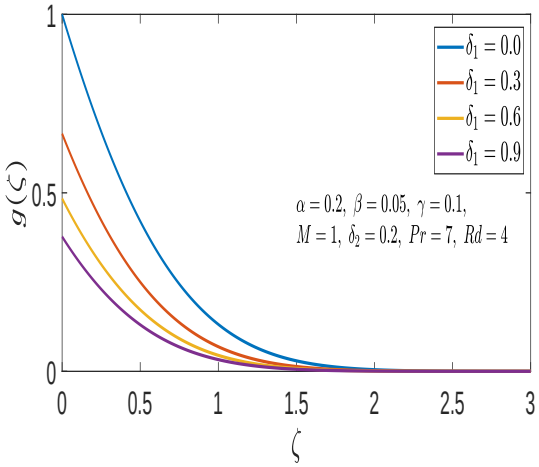

Figure 5: Velocity profile $g(\zeta)$ for various values of velocity slip parameter δ_1.

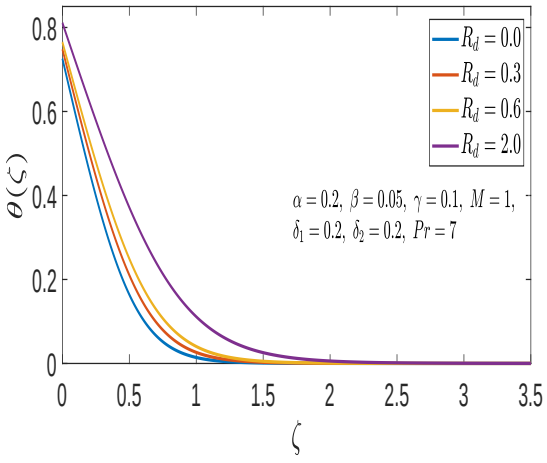

Figure 6: $\theta(\zeta)$ for various values of radiation parameter Rd.

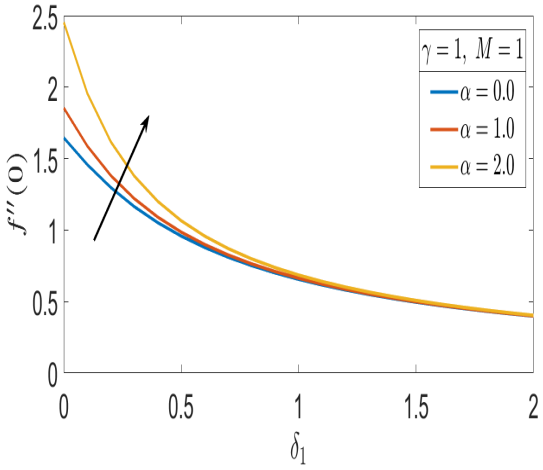

Figure 7: $f''(0)$ against δ_1 for different values of α.

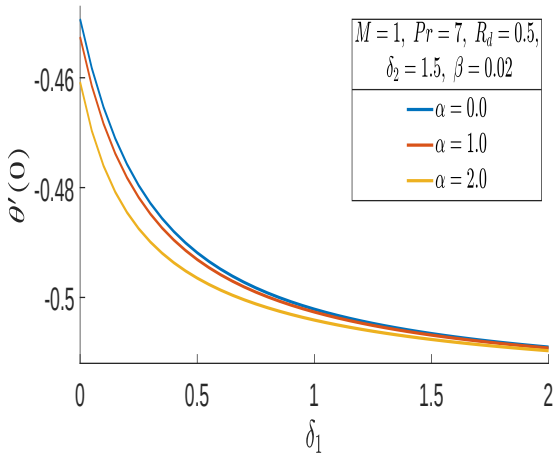

Figure 8: $\theta'(0)$ for variable rotation ratio parameter α against slip parameter δ_1.

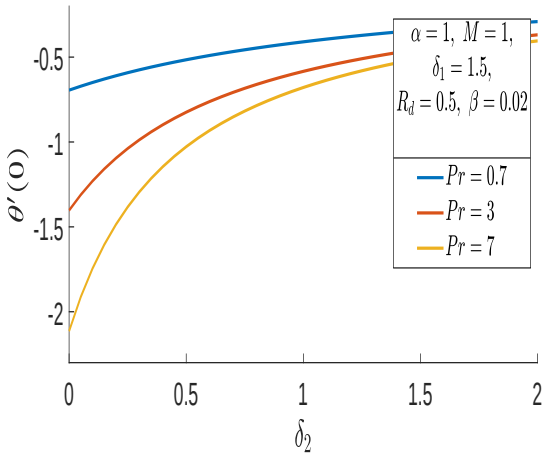

Figure 9: Local heat flux $\theta'(0)$ against momentum slip parameter δ_2 for various values of Prandtl number Pr.

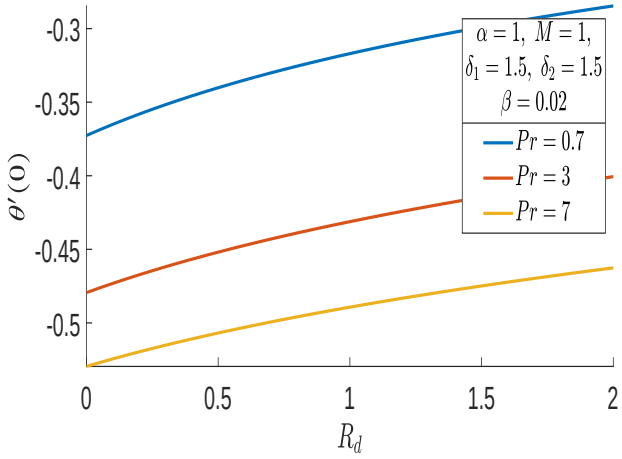

Figure 10: Local heat flux $\theta'(0)$ against radiation parameter R_d for various values of Prandtl number Pr.

4 Conclusion

MHD Oblique flow towards a rotating disk in the presence of velocity and thermal slip conditions has been modelled, transformed, and examined. Thermal radiation and thermal relaxation effects are also taken into consideration. The core outcomes of the study are summarized as:

The point of stagnation varies a bit with an increase in the velocity slip. The existence of rotational movement on the disk surface is evident when there is a velocity slip. The velocity slip parameter increases, and the velocity of the main flow increases, while the velocity of the cross-flow decreases. The profile of temperature is lowered because of the joint effects of temperature in the boundary layer and heat radiation. The friction of the skin on the disk surface also reduces with the velocity slip, but mass rises with the stronger rotational effect. In addition, the local heat transfer through the rotating disk is enhanced by increased parameters of thermal slip and thermal radiation. To further the study, transient effects and behavior of non-Newtonian fluids would be of interest in studying the slip flows in rotating disks in the future. To bridge the gap between theory and practice, experimental research and practical implementation in the design of rotating machinery would be beneficial. More effective slip and thermal control could improve thermal control and be useful in advanced engineering devices.

Acknowledgement: Not applicable.

Funding Statement: The authors received no specific funding for this study.

Author Contributions: The authors confirm contribution to the paper as follows: Conceptualization, Abdou Alzubaidi, Rashid Mehmood; methodology, Khalid Mahmud, Siddra Rana; software, Rashid Mehmood; validation, Abdou Alzubaidi, Rashid Mehmood; formal analysis, Siddra Rana; investigation, Abdou Alzubaidi; resources, Rashid Mehmood; data curation, Mohammed Alkinidri, Siddra Rana; writing original draft preparation, Khalid Mahmud; writing review and editing, Siddra Rana; visualization, Rashid Mehmood; supervision, Rashid Mehmood; project administration, Mohammed Alkinidri. All authors reviewed and approved the final version of the manuscript.

Availability of Data and Materials: The authors confirm that the data supporting the findings of this study are available within the article. The data that support the findings of this study are available from the Corresponding Author, [Rashid Mehmood], upon reasonable request.

Ethics Approval: Not applicable.

Conflicts of Interest: The authors declare no conflicts of interest.

Nomenclature

B_0	uniform external magnetic field (Tesla)	BCs	boundary Conditions
BVP	boundary value problem	Bi	Biot number
c	specific heat	h	induced velocity function
$h'(0)$	tangential component of surface	$f''(0)$	skin friction
IVP	initial value Problem	M	magnetic flux parameter
ODEs	Ordinary differential equations	PDEs	Partial differential equations
P	pressure	Pr	Prandtl number
q	heat flux	R_d	thermal radiation
T	fluid's temperature	u	x-component of fluid's velocity
v	y-component of fluid's velocity	z	an axis normal to rotating disk
α	rotational ratio	β	thermal relaxation parameter
γ	obliqueness parameter	δ_1	velocity slip parameter
δ_2	thermal slip parameter	θ	Temperature
ν	kinematic viscosity	ρ	density
κ	Thermal conductivity	Ω	angular velocity

Appendix A Solution Methodology

Researchers have proposed a variety of approaches to deal with nonlinear systems, including the Keller box method, finite difference approach, and shooting method, which are significant. To find a solution in this situation, the set of coupled non-linear Eqs. (18)–(21) along consistent BCs (22) and (23) are numerically solved using built-in MATLAB code BVPC, which is the RK method inconsistent with the shooting technique [43]. BVP4C can be written as an explicit Runge–Kutta formulation with continuous extensions or as a collocation approach utilizing C1 piecewise cubic polynomials. Eqs. (18)–(21) with (22) and (23) were changed into different equations by applying sequential transformations.

$$\left.\begin{aligned} &w_1 = f(\zeta), w_2 = w_1' = f'(\zeta), w_3 = w_2' = f''(\zeta), w_4 = w_3' = f'''(\zeta)\\ &w_5 = g(\zeta), w_6 = w_5' = g'(\zeta), w_7 = w_6' = g''(\zeta)\\ &w_8 = h(\zeta), w_9 = w_8' = h'(\zeta), w_{10} = w_9' = h''(\zeta)\\ &w_{11} = \theta(\zeta), w_{12} = w_{11}' = \theta'(\zeta), w_{13} = w_{12}' = \theta''(\zeta) \end{aligned}\right\} \tag{A1}$$

$$w_3' = -2w_1w_3 + w_2^2 - 1 - \alpha^2 w_5^2 - M^2 + M^2 w_2 \tag{A2}$$

$$w_6' = -2w_1w_6 + 2w_5w_2 + M^2 w_5 \tag{A3}$$

$$w_9' = -2w_1w_9 + w_8w_2 + M^2 w_8 - M^2 \gamma \zeta^{\frac{1}{2}} \tag{A4}$$

$$w_{12}' = \frac{1}{(1+R_d)} \Pr\left[-2w_1w_{12} + 4\beta[w_1w_2w_{12} + w_2^2 w_{13}]\right] \tag{A5}$$

$$\left.\begin{aligned} &w_1(0)=0, w_2(0)=\alpha_1, w_5(0)=0, w_8(0)=\alpha_2,\\ &w_6(0)=0, w_7(0)=\alpha_3, w_9(0)=0, w_10(0)=\alpha_4,\\ &w_{11}(0)=\alpha_5, w_{12}(0)=w_{11}(0)=\alpha_6, w_{13}(0)=\alpha_7 \end{aligned}\right\} \tag{A6}$$

where $\alpha_i, i = 1, 2, 3 \ldots$ are the shooting parameters. A four-decimal-place tolerance level is selected for all numerical schemes. Here flowchart (Fig. A1) of the numerical scheme until convergence is achieved.

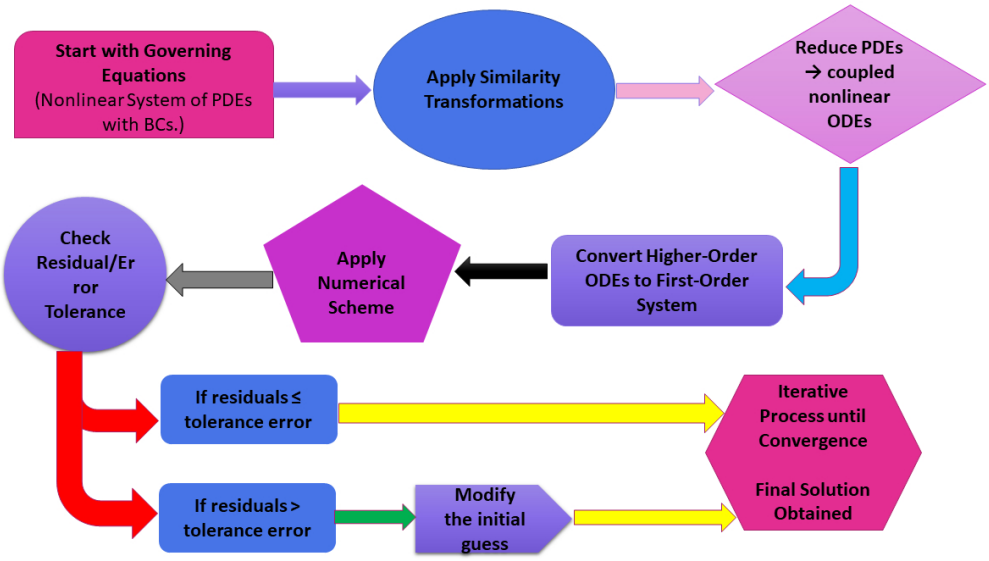

Figure A1: Solution methodology.

The nonlinear boundary-value problem has a mixed shooting-BVP4C solution. By integrating the ODE system of the form $\eta = 0$, a truncated boundary $\eta \to \infty$ with tolerances $RelTol = 10^{-8}$ and $AbsTol = 10^{-10}$, the shooting step provides accurate initial estimates of the missing slope of the boundaries. The MATLAB collocation solver BVP4C receives these initial guesses and uses adaptive mesh control $RelTol = 10^{-6}$ and $AbsTol = 10^{-8}$, $NMax = 5000$ to refine the result. The hybrid solver provides stability and accuracy because a pure shot technique is highly sensitive to early predictions, and a pure BVP solver may not converge without a solid beginning profile. The computational domain is where the truncation point is located. The combined methodology guarantees both stability and accuracy because a pure shooting method is very sensitive to beginning predictions, and a pure BVP solution may fail without a strong starting profile. Depending on the parameter configuration, the computational domain is truncated at η_∞ = 15–20. Grid-independent values of $f''(0)$, $g'(0)$ and $\theta'(0)$ with changes below, 10^{-6} are confirmed by mesh refinement tests with 100, 200, and 400 points. Mesh independence checks, residual tolerance, and boundary-condition satisfaction η_∞ are used to confirm convergence.

References

1. Von Kármán T. Uber laminare und turbulente reibung. Z Angew Math Mech. 1921;1:233–52. (In German). [CrossRef].
2. Lok Y, Amin N, Pop I. Non-orthogonal stagnation point flow towards a stretching sheet. Int J Non-Linear Mech. 2006;41(4):622–7. [CrossRef].

3. Nadeem S, Mehmood R, Akbar NS. Non-orthogonal stagnation point flow of a nano non-Newtonian fluid towards a stretching surface with heat transfer. Int J Heat Mass Transf. 2013;57(2):679–89. [CrossRef].
4. Mehmood R, Nadeem S, Saleem S, Akbar NS. Flow and heat transfer analysis of Jeffery nano fluid impinging obliquely over a stretched plate. J Taiwan Inst Chem Eng. 2017;74:49–58. [CrossRef].
5. Sarkar S, Sahoo B. Oblique stagnation flow towards a rotating disc. Eur J Mech-B/Fluids. 2021;85:82–9. [CrossRef].
6. Ahmed J, Khan M, Ahmad L. Stagnation point flow of Maxwell nanofluid over a permeable rotating disk with heat source/sink. J Mol Liq. 2019;287:110853. [CrossRef].
7. Hafeez A, Khan M, Ahmed J. Stagnation point flow of radiative Oldroyd-B nanofluid over a rotating disk. Comput Methods Programs Biomed. 2020;191:105342. [CrossRef].
8. Mahanthesh B, Gireesha B, Shehzad S, Rauf A, Kumar PS. Nonlinear radiated MHD flow of nanoliquids due to a rotating disk with irregular heat source and heat flux condition. Phys B Condens Matter. 2018;537:98–104. [CrossRef].
9. Andersson HI, Rousselet M. Slip flow over a lubricated rotating disk. Int J Heat Fluid Flow. 2006;27(2):329–35. [CrossRef].
10. Imtiaz M, Hayat T, Alsaedi A, Asghar S. Slip flow by a variable thickness rotating disk subject to magnetohydrodynamics. Results Phys. 2017;7:503–9. [CrossRef].
11. Mustafa M. MHD nanofluid flow over a rotating disk with partial slip effects: Buongiorno model. Int J Heat Mass Transf. 2017;108:1910–6. [CrossRef].
12. Wang R, Chai J, Luo B, Liu X, Zhang J, Wu M, et al. A review on slip boundary conditions at the nanoscale: Recent development and applications. Beilstein J Nanotechnol. 2021;12(1):1237–51. [CrossRef].
13. Naqvi SMRS, Kim HM, Muhammad T, Mallawi F, Ullah MZ. Numerical study for slip flow of Reiner-Rivlin nanofluid due to a rotating disk. Int Commun Heat Mass Transf. 2020;116:104643. [CrossRef].
14. Majeed AH, Jan AZ, Alamri AM, Alqahtani SA, Ali MR, Hendy AS. Recent developments in the Darcy-Forchheimer model of magnetized tetra hybrid nanofluid activation energy/joule heating in a stenotic artery. Case Stud Therm Eng. 2024;59:104346. [CrossRef].
15. Khan MI, Waqas H, Khan SU, Imran M, Chu Y-M, Abbasi A, et al. Slip flow of micropolar nanofluid over a porous rotating disk with motile microorganisms, nonlinear thermal radiation and activation energy. Int Commun Heat Mass Transf. 2021;122:105161. [CrossRef].
16. Shoaib M, Raja M, Sabir M, Nisar K, Jamshed W, Felemban B, et al. MHD hybrid nanofluid flow due to rotating disk with heat absorption and thermal slip effects: An application of intelligent computing. Coatings. 2021;11:1554. [CrossRef].
17. Zemedu C, Ibrahim W. Nonlinear convection flow of micropolar nanofluid due to a rotating disk with multiple slip flow. Math Probl Eng. 2020;2020(1):4735650. [CrossRef].
18. Rafiq MY, Sabeen A, ur Rehman A, Abbas Z. Comparative study of Yamada-Ota and Xue models for MHD hybrid nanofluid flow past a rotating stretchable disk: Stability analysis. Int J Numer Methods Heat Fluid Flow. 2024;34(10):3793–819. [CrossRef].
19. Turkyilmazoglu M. Nanofluid flow and heat transfer due to a rotating disk. Comput Fluids. 2014;94:139–46. [CrossRef].
20. Abbas Z, Rafiq M, Hasnain J, Nadeem A. Thermally developed generalized Bödewadt flow containing nanoparticles over a rotating surface with slip condition. Int Commun Heat Mass Transf. 2021;122:105143. [CrossRef].
21. Khedher NB, Ijaz N, Medani M, Barghout K, Abu-Libdeh N. Electro-osmotic transport and thermal energy dynamics of tetra-hybrid nano fluid in complex peristaltic flows. Case Stud Therm Eng. 2024;57:104317. [CrossRef].
22. Siddiqui BK, Batool S, Malik M, ul Hassan QM, Alqahtani AS. Darcy Forchheimer bioconvection flow of Casson nanofluid due to a rotating and stretching disk together with thermal radiation and entropy generation. Case Stud Therm Eng. 2021;27:101201. [CrossRef].
23. Song Y-Q, Khan SA, Imran M, Waqas H, Khan SU, Khan MI, et al. Applications of modified Darcy law and nonlinear thermal radiation in bioconvection flow of micropolar nanofluid over an off centered rotating disk. Alex Eng J. 2021;60(5):4607–18. [CrossRef].
24. Fourier JBJ. Théorie analytique de la chaleur. Paris, France: Gauthier-Villars et fils; 1888. (In French).

25. Cattaneo C. Sulla conduzione del calore. Atti Sem Mat Fis Univ Modena. 1948;3:83–101. (In Italian).
26. Christov C. On frame indifferent formulation of the Maxwell–Cattaneo model of finite-speed heat conduction. Mech Res Commun. 2009;36(4):481–6. [CrossRef].
27. Doh D-H, Cho G-R, Ramya E, Muthtamilselvan M. Cattaneo-Christov heat flux model for inclined MHD micropolar fluid flow past a non-linearly stretchable rotating disk. Case Stud Therm Eng. 2019;14:100496. [CrossRef].
28. Saeed M, Mansoor M, Arshad HZ, Shahzad M. Bayesian regularization artificial neural network approach for numerical modelling of Maxwell nanofluid flow across a stretch sheet: Examine the effects of chemical reactions and heat radiation. Nonlinear Dyn. 2025;113(19):26145–63. [CrossRef].
29. Gholinia M, Hosseinzadeh K, Ganji D. Investigation of different base fluids suspend by CNTs hybrid nanoparticle over a vertical circular cylinder with sinusoidal radius. Case Stud Therm Eng. 2020;21:100666. [CrossRef].
30. Imtiaz M, Kiran A, Hayat T, Alsaedi A. Axisymmetric flow by a rotating disk with Cattaneo–Christov heat flux. J Braz Soc Mech Sci Eng. 2019;41(3):149. [CrossRef].
31. Tulu A, Ibrahim W. MHD slip flow of CNT-ethylene glycol nanofluid due to a stretchable rotating disk with Cattaneo–Christov heat flux model. Math Probl Eng. 2020;2020(1):1374658. [CrossRef].
32. Hafeez A, Khan M, Ahmed J. Flow of Oldroyd-B fluid over a rotating disk with Cattaneo–Christov theory for heat and mass fluxes. Comput Methods Programs Biomed. 2020;191:105374. [CrossRef].
33. Mehmood R, Noreena, Rana S, Akbar NS, Zidan AM. Thermally stratified electrically conducting flow interacting MWCNT/SWCNT hybrid nanofluid over an inclined riga plate with variable viscosity and thermal slip: Application in nanotechnology. J Therm Anal Calorim. 2025;150(5):3751–65. [CrossRef].
34. Ali I, Mehmood R, Sarkar S, Muhammad T, Riaz M, Gharib M, et al. MHD oblique flow of variable viscosity nanofluid (CuO+ H2O) over a rotating disk. ZAMM J Appl Math Mech. 2025;105(5):e70033. [CrossRef].
35. Alkuhayli NAM. Magnetohydrodynamic flow of Copper-Water nanofluid over a rotating rigid disk with Ohmic heating and Hall Effects. J Magn Magn Mater. 2023;575:170709. [CrossRef].
36. Vijay N, Sharma K. Magnetohydrodynamic hybrid nanofluid flow over a decelerating rotating disk with Soret and Dufour effects. Multidiscip Model Mater Struct. 2023;19(2):253–76. [CrossRef].
37. Chandra Sekar Reddy R, Reddy PS, Sreedevi P. Impact of the Cattaneo–Christov heat flux on heat and mass transfer analysis of a hybrid nanofluid flow over a vertical cone. Int J Ambient Energy. 2022;43(1):6919–31. [CrossRef].
38. Turkyilmazoglu M. Wall stretching in magnetohydrodynamics rotating flows in inertial and rotating frames. J Thermophys Heat Transf. 2011;25(4):606–13. [CrossRef].
39. Childs P. Rotating flow. Amsterdam, The Netherlands: Elsevier; 2010.
40. Cochran W, editor. The flow due to a rotating disc. In: Mathematical proceedings of the Cambridge philosophical society. Cambridge, UK: Cambridge University Press; 1934.
41. Mehmood A, Usman M. Heat transfer enhancement in rotating disk boundary layer. Therm Sci. 2018;22(6 Part A):2467–82. [CrossRef].
42. Shevchuk IV. Convective heat and mass transfer in rotating disk systems. Berlin/Heidelberg, Germany: Springer; 2009.
43. Shampine LF, Gladwell I, Thompson S. Solving ODEs with matlab. Cambridge, UK: Cambridge University Press; 2003.